

Automated Retinal Layer and Fluid Segmentation and Cross-sectional Analysis using Spectral Domain Optical Coherence Tomography Images for Diabetic Retinopathy

Shuo Chen¹, Da Ma², Munispriyan Raviselvan³, Sathishkumar Sundaramoorthy³, Karteek Popuri⁷, Meyong Jin Ju⁴, Marinko V. Sarunic^{5,6}, Dhanashree Ratra³, and Mirza Faisal Beg¹

¹ School of Engineering Science, Simon Fraser University, Burnaby, BC, Canada

² School of Medicine, Wake Forest University, Winston-Salem, NC, United States

³ Sankara Nethralaya, Chennai, Tamil Nadu, India

⁴ Department of Ophthalmology & Visual Sciences, The University of British Columbia, Vancouver, BC, Canada

⁵ Institute of Ophthalmology, University College London, London, United Kingdom

⁶ Department of Medical Physics and Biomedical Engineering, University College London, London, United Kingdom

⁷ Memorial University of New Foundland, Department of Computer Science, St. Johns, Canada

Background: Diabetic retinopathy is a leading microvascular complication of diabetes and a significant cause of vision loss. Without timely intervention, it can lead to irreversible blindness. Spectral Domain Optical Coherence Tomography enables high-resolution imaging of retinal structures, aiding in the early detection of pathological changes. AI-driven segmentation enhances diagnostic precision and reduces clinician workload. This study aims to develop a deep learning-based pipeline for automated retinal segmentation and thickness analysis to improve DR assessment and monitoring.

Methods: A deep neural network was trained for automated segmentation of ten retinal layers, intra-retinal fluid, and hyperreflective foci. Initial manual annotations from five SD-OCT volumes were used to train the model, with iterative refinements improving accuracy. Performance was evaluated using five-fold cross-validation across four DNN architectures. Retinal thickness was measured via the K-nearest neighbours algorithm, and Early Treatment Diabetic Retinopathy Study maps visualized spatial variations. Statistical comparisons were made between Non-Proliferative and Proliferative Diabetic Retinopathy. The correlation between layer thickness and visual acuity within each DR group is also evaluated.

Results: SwinUNETR achieved the highest segmentation accuracy, with a Dice Similarity Coefficient of 0.7719 and a Normalized Surface Dice of 0.8149. VM-Unet showed superior DSC performance in specific layers (Vitreous, RNFL, GCL+IPL, ONL+IS), while SwinUNETR excelled in EZ, OS, RPE, and HRF regions. The predicted segmentation can be used to produce comparable thickness measurements with ground truth. PDR patients exhibited increased layer thickness in the SO sector of OPL, plus fluid and HRF accumulation in the SO and TO sectors, respectively. Whereas NPDR showed greater thickness in multiple sectors of ONL+IS. Several sectors of ONL+IS, EZ, OS and RPE show a positive correlation between layer thickening and worse vision. The accumulation of both fluid and HRF is also significantly correlated with vision decline.

Conclusion: This study introduces an AI-based pipeline for automated DR assessment. It reduces manual annotation effort while maintaining high accuracy. The generated thickness maps provide valuable clinical insights, supporting disease monitoring and treatment planning.

Index Terms—Optical Coherence Tomography; Diabetic Retinopathy; Layer and fluid segmentation; Retinal thickness Analysis;

I. INTRODUCTION

Diabetic retinopathy (DR) is a prevalent microvascular complication of diabetes mellitus (DM) and a leading cause of vision impairment worldwide (Klein, 2007). It is estimated that approximately 20% of diabetic individuals over the age of 50 will develop DR, which, if left untreated, can progress to severe visual impairment or blindness (Teo et al., 2021). The progression of DR is influenced by several risk factors, including prolonged diabetes duration, elevated glycated hemoglobin (HbA1c) levels, hypertension, hyperlipidemia, obesity, and smoking (Klein et al., 2014)(Zhou et al., 2025)(Mori et al., 2024)(Cheung et al., 2016)(Zhang et al., 2024)(Cao et al., 2017). Clinically, DR is categorized into two primary stages: Non-Proliferative Diabetic Retinopathy (NPDR) and Proliferative Diabetic Retinopathy (PDR). NPDR represents an early stage, often asymptomatic, characterized by microvascular abnormalities that progressively compromise retinal capillary integrity. Without timely medical intervention, NPDR can advance to PDR, a more severe stage marked by pathological neovascularization due to chronic retinal ischemia. This progression increases the risk of severe complications such as vitreous hemorrhage and retinal detachment, ultimately threatening vision.

Spectral Domain Optical Coherence Tomography (SD-OCT) is a cutting-edge, non-invasive imaging technique that provides high-resolution, cross-sectional visualization of retinal structures. Its real-time image acquisition capability makes it an invaluable tool for DR screening and early diagnosis (Gabriele E. Lang, 2007). SD-OCT enables the detection of subclinical retinal changes by quantifying variations in retinal thickness and identifying fluid accumulation. Accurate and reliable segmentation of retinal layers and pathological features is crucial for DR diagnosis and treatment planning. Figure 1 illustrates a representative SD-OCT B-scan with retinal

layer and fluid segmentation. The segmentation delineates nine essential retinal layers: the Retinal Nerve Fiber Layer (RNFL), Ganglion Cell Layer and Inner Plexiform Layer (GCL+IPL), Inner Nuclear Layer (INL), Outer Plexiform Layer (OPL), Outer Nuclear Layer and Inner Segment Layer (ONL+IS), Ellipsoid Zone (EZ), Outer Segment Layer (OS), and Retinal Pigment Epithelium (RPE). The region above the Internal Limiting Membrane (ILM) is also identified as the Vitreous, while the Choroid lies beneath Bruch's Membrane (BM). Fluid segmentation involves three primary fluid types: intraretinal fluid (IRF), subretinal fluid (SRF), and pigment epithelial detachment (PED), all of which appear as hypo-reflective regions between the ILM and BM. Furthermore, hyperreflective foci (HRF), which manifest as high-intensity dot-like or clustered lesions, are also segmented.

Numerous studies have explored automated segmentation techniques for retinal layer analysis. Herzog *et al.* proposed an edge maximization and smoothness-constrained thresholding approach to delineate retinal boundaries (Herzog *et al.*, 2004). Chiu *et al.* utilized a graphical cut algorithm to minimize the weighted sum of edge paths along connected nodes, effectively segmenting retinal layers (Chiu *et al.*, 2010). Wang *et al.* introduced a multi-step approach that includes artifact removal, contrast enhancement, and segmentation via level set methods, k-means clustering, and Markov random fields (MRFs) (Wang *et al.*, 2015). Traditional machine-learning techniques have also been employed for fluid segmentation. González *et al.* identified dark fluid regions in OCT scans using support vector machines (SVM) and random forest classifiers (Gonzalez *et al.*, 2013). Chen *et al.* applied a graph-cut classifier followed by a region-growing algorithm for cystoid macular edema (CME) segmentation (Xinjian Chen *et al.*, 2012). However, these conventional approaches are limited by their reliance on handcrafted features and their susceptibility to performance degradation in severely diseased cases.

Deep learning has emerged as a powerful alternative for automated retinal segmentation, offering greater robustness against variations in image quality and pathological abnormalities. Liu *et al.* utilized a ResNet-based convolutional neural network (CNN) combined with a random forest classifier for patch-wise layer segmentation (Liu *et al.*, 2019). Kugelman *et al.* proposed a recurrent neural network (RNN) with a graph search framework to segment retinal layers in both healthy individuals and patients with age-related macular degeneration (AMD) (Kugelman *et al.*, 2018). Hu *et al.* developed a multi-scale CNN capable of capturing different feature levels for improved segmentation accuracy (Hu *et al.*, 2019). U-Net and its derivatives have become widely adopted among deep-learning models for medical image segmentation. U-Net's encoder-decoder architecture, enhanced by skip connections, enables efficient spatial information preservation and mitigates vanishing gradient issues (Ronneberger *et al.*, 2015). It has been successfully applied to retinal layer segmentation, fluid detection, and HRF analysis, achieving state-of-the-art (SOTA) performance (Roy *et al.*, 2017)(Ma *et al.*, 2021)(Tennakoon *et al.*, 2018)(Schlegl *et al.*, 2018). More recently, Vision Transformers (ViTs) have outperformed CNNs in large-scale datasets. Unlike CNNs, which rely on local

receptive fields, ViTs employ self-attention mechanisms to capture global dependencies, which is particularly beneficial for detecting diffuse fluid regions. Xue *et al.* implemented a Swin-Transformer-based architecture for fluid segmentation in diabetic macular edema (DME) and AMD, demonstrating superior performance over traditional CNN-based models (Xue and Du, 2024). Kulyabin *et al.* leveraged the Segment Anything Model (SAM) for retinal fluid segmentation, incorporating point and bounding box prompts to outperform U-Net in macular hole and fluid segmentation tasks (Kulyabin *et al.*, 2024). Despite these advancements, most existing studies focus on either the retinal layer or fluid segmentation, with limited efforts dedicated to integrating segmentation outcomes with clinical statistical analysis.

Several studies have examined the relationship between retinal layer thickness, fluid accumulation, and DR severity. Browning *et al.* analyzed macular thickness across different DR severity levels and observed a correlation between macular thickening and increased risk of subclinical edema (Browning *et al.*, 2008). Kim *et al.* investigated choroidal thickness alterations in DR and DME patients, reporting a significant increase in choroidal thickness as DR severity progressed from mild/moderate NPDR to PDR (Kim *et al.*, 2013). Cho *et al.* assessed macular and peripapillary retinal thickness in DR subjects, identifying statistically significant differences in retinal thickness across seven anatomical regions between DR and control groups (Cho *et al.*, 2010). Santos *et al.* demonstrated that fluid accumulation within the outer segment (OS) layer was significantly associated with central retinal thickness and visual impairment in DME patients (Santos T *et al.*, 2024). These findings suggest that retinal layer thickness and fluid distribution are reliable biomarkers for DR diagnosis and progression monitoring.

This study introduces a fully automated pipeline integrating retinal layer and fluid segmentation with a statistical analysis of structural changes in DR patients. The key contributions include:

- 1) Development of a scalable pipeline for large-scale manual segmentation refinement.
- 2) Quantitative evaluation of multiple SOTA deep learning models for retinal layer and fluid segmentation.
- 3) Cross-sectional analysis of retinal structural changes and demographic variations, providing clinically relevant insights into DR progression.

II. METHODS

A. Data Acquisition

116 SD-OCT volumes were acquired from Sankara Nethralaya Eye Care Hospital in India. The imaging data was obtained using the Cirrus HD-OCT 5000 (Carl Zeiss Meditec, Dublin, CA, USA). Seventeen OCT volumes were captured in Macular Cube mode with a 512×128 pixels resolution, covering a 6×6 mm² macular region centered on the fovea. The remaining 99 volumes were scanned in OCTA mode at 350×350 pixels, covering a 6×6 mm² macular region. Despite differences in scanning speed and resolution, Wong *et al.* reported no significant variation in macular thickness

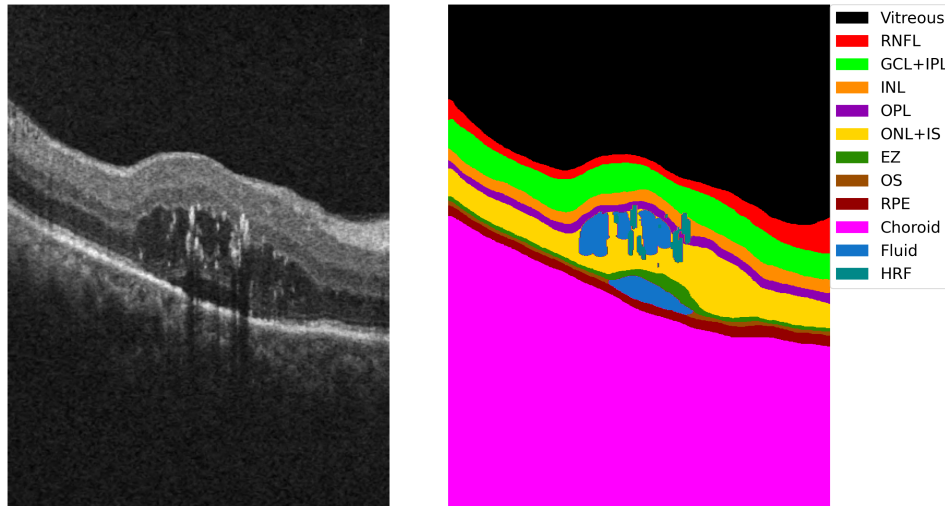


Fig. 1: Example of retinal OCT segmentation(image on the right) for a single B-scan(image on the left). This image is acquired from a 59-year-old female patient with NPDR. Ten retinal layers are segmented from top to bottom, plus the fluid and HRF within the retinal body.

measurements between the two modes (Wong et al., 2024). Table I presents the demographic details of the two DR groups, showing no significant differences in age, diabetes duration, or visual acuity ($p > 0.05$). However, the gender distribution differs due to the limited number of female patients in the PDR group.

B. Pre-processing

To prepare the raw OCT volumes for further analysis, we perform several pre-processing steps:

- The approximate retinal center in each B-scan is adjusted to align with the center along the axial direction. The axial retinal center is estimated by computing the average axial position of pixels whose axial intensity values are more significant than the lowest 20th percentile. This helps initialize a starting point for axial motion correction.
- A 3D Bounded Variation (BV) smoothing technique is applied to suppress noise while preserving sharp structural boundaries. This provides a better contrast between manual labelling and correction.
- Motion artifacts are corrected in each B-scan’s axial and lateral directions. Axial translations are determined through cross-registration using the moving average of the central B-scan as a reference. Lateral corrections are achieved by performing registration based on the adjacent B-scans’ discrete Fourier transform (DFT). Rotational adjustments are computed by transforming translations into polar space, using the moving average of the central B-scan as a reference.

C. Manual Segmentation

Figure 2 illustrates that the segmentation process follows a structured workflow. Initially, five volumes are manually annotated from scratch. To enhance efficiency, manual segmentation is performed on every fifth B-scan, while the intermediate B-scans are interpolated under the assumption that adjacent B-scans share structural similarities. However, B-scans that

exhibit significant structural changes are individually labelled. These five manually labelled volumes serve as the initial training dataset for a deep neural network (DNN), which is trained using a data split ratio of 3:1:1 for training, validation, and testing. The trained model is then used to generate segmentation predictions for an additional 20 volumes, which are subsequently reviewed and manually corrected. This iterative process continues, with the network being retrained on an expanded dataset each time, ensuring that all volumes undergo accurate segmentation and manual verification.

D. Networks

We investigate the performance of four deep neural network (DNN) architectures, which are either widely used for medical image segmentation or have demonstrated state-of-the-art (SOTA) performance in related tasks:

- **U-Net:** A well-established medical image segmentation model that employs an encoder-decoder architecture with skip connections (Ronneberger et al., 2015). While effective, it may struggle with high-resolution inputs due to a lack of global contextual awareness.
- **SegFormer:** Designed by Xie *et al.*, this framework utilizes a hierarchical transformer encoder combined with a lightweight MLP decoder to enhance feature extraction (Xie et al., 2021).
- **SwinUNETR:** Proposed by Hatamizadeh *et al.*, this architecture replaces the CNN-based encoder in U-Net with a Swin Transformer encoder, enabling multi-scale feature extraction through a shifted windowing mechanism (Hatamizadeh et al., 2022).
- **VM-UNet:** Developed by Ruan *et al.*, this model introduces a state-space model (SSM) and an asymmetric encoder-decoder structure, balancing computational efficiency while maintaining a global contextual view (Ruan et al., 2024).

The U-Net model is configured with a depth of five channels and three residual units. The 2D variant of SwinUNETR is

Group	N	Age (Mean \pm SD)	Gender	Duration of Diabetes (yrs)	Visual Acuity (LogMAR)
NPDR	66	60.00 \pm 8.85	Female: 34, Male: 32	15.94 \pm 7.97	0.35 \pm 0.35
PDR	50	56.84 \pm 8.24	Female: 13, Male: 37	14.66 \pm 8.60	0.47 \pm 0.41
p-value	-	0.05023	0.00457	0.41508	0.10351

TABLE I: Demographic information of experimental DR groups. Numerical values are presented as mean \pm standard deviation (SD). The visual acuity is expressed in the logarithm of the Minimum Angle of Resolution (LogMAR). The p-values are calculated using the Student's t-test.

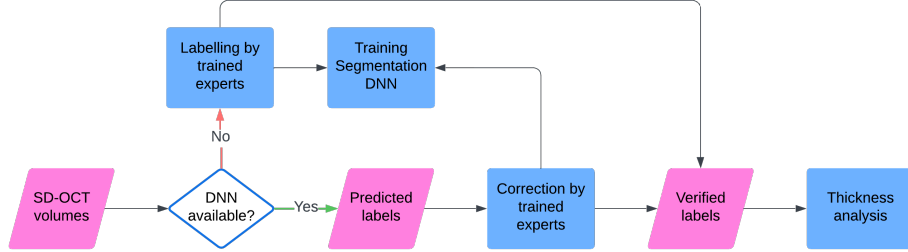


Fig. 2: Manual segmentation pipeline. Multiple iterations were performed between DNN training and manual corrections. A thickness analysis was conducted after segmentation had been completed and verified.

used for training B-scans. The architectures of the remaining three networks are adopted as described in their original publications. The VM-UNet model is initialized using VMamba-S, pre-trained on the ImageNet-1k dataset (Liu et al., 2024).

E. Training Settings

We employed 5-fold cross-validation, stratified by DR diagnosis, with a 4:1:1 ratio for training, validation, and testing. Each input consisted of a 3-channel image constructed by three repetitions of a single B-scan. Each training B-scan is resized to 512×512 . To mitigate class imbalance, excess Vitreous and Choroid regions were cropped. Various augmentation techniques are applied, including lateral flipping, Gaussian noise addition, contrast enhancement, rotation within the B-scan plane, and random intensity shifting.

For loss functions, we use the combinations of Dice loss, cross-entropy (CE) loss, and the L1 loss of texture differences. Given the ground truth label y and predicted label \hat{y} , for every pixel i , the Dice loss is calculated as:

$$L_{dice}(y, \hat{y}) = 1 - \frac{2 \cdot \sum_i y_i \hat{y}_i}{\sum_i y_i^2 + \sum_i \hat{y}_i^2 + \epsilon} \quad (1)$$

We set ϵ to 10^{-6} to avoid the division by zero problem. The CE loss is defined as:

$$L_{CE}(y, \hat{y}) = -\frac{1}{N} \sum_i [y_i \log(\hat{y}_i) + (1 - y_i) \log(1 - \hat{y}_i)] \quad (2)$$

The Sobel operator calculates gradients in horizontal(G_x) and vertical(G_y) directions, and the total gradient magnitude G is the Euclidean norm. Given the label Y , the gradients are calculated as:

$$G_x(Y) = Y * \begin{bmatrix} -1 & 0 & 1 \\ -2 & 0 & 2 \\ -1 & 0 & 1 \end{bmatrix}, \quad G_y(Y) = Y * \begin{bmatrix} -1 & -2 & -1 \\ 0 & 0 & 0 \\ 1 & 2 & 1 \end{bmatrix}$$

$$G(Y) = \sqrt{G_x(Y)^2 + G_y(Y)^2} \quad (3)$$

The texture loss is defined as the L1 norm between the predicted and ground truth labels:

$$L_{texture}(y, \hat{y}) = \frac{1}{N} \sum_i |G_i(y) - G_i(\hat{y})| \quad (4)$$

Thus, the total loss function is calculated as:

$$L(y, \hat{y}) = \alpha \cdot L_{dice} + \beta \cdot L_{CE} + \gamma \cdot L_{texture} \quad (5)$$

The α , β , and γ are weighting factors for Dice, CE and texture losses, respectively. We empirically set $\alpha = \beta = \gamma = 1$ for our experiment.

We empirically assign different class weights to CE loss to emphasize the class imbalance issue. Specifically, we assign 0.1 to Vitreous and Choroid, 0.5 to the rest of the layers, and 1 to fluid and HRF. We use AdamW optimizer with CosineAnnealing scheduler with the warm restart. We use the distributed parallel learning supported by the PyTorch Lightning module¹, with a batch size of 8 and a learning rate of $1e-4$. The training is deployed on NVIDIA V100 Volta GPU allocated by Cedar Compute Canada².

F. Evaluation Metrics

We evaluate the segmentation performance by overlapping areas and boundary alignment. We use the Dice similarity coefficient (DSC) to measure the similarity between the predicted and ground truth masks. Given correctly predicted pixels as True Positives(TP), incorrectly predicted pixels as False Positives(FP), and missing predicted pixels as False Negatives(FN), the Dice score is calculated as:

¹<https://lightning.ai/>

²More information can be found at: <https://docs.alliancecan.ca/wiki/Cedar>

$$Dice = \frac{2 \cdot TP}{2 \cdot TP + FP + FN} \quad (6)$$

Nikolov *et al.* proposed the normalized surface Dice (NSD) to estimate the deviation of surface contours within a certain threshold τ (Nikolov et al., 2018). Defining a set of Euclidean distances from predicted segmentation \hat{Y} to ground truth segmentation Y as $\mathcal{D}_{\hat{Y}Y}$, and vice versa as $\mathcal{D}_{Y\hat{Y}}$, we obtain the subset of distances that are smaller or equal to the threshold τ as:

$$\begin{aligned} \mathcal{D}'_{\hat{Y}Y} &= \{d \in \mathcal{D}_{\hat{Y}Y} | d \leq \tau\} \\ \mathcal{D}'_{Y\hat{Y}} &= \{d \in \mathcal{D}_{Y\hat{Y}} | d \leq \tau\} \end{aligned} \quad (7)$$

The NSD is calculated as :

$$NSD = \frac{|\mathcal{D}'_{\hat{Y}Y}| + |\mathcal{D}'_{Y\hat{Y}}|}{|\mathcal{D}_{\hat{Y}Y}| + |\mathcal{D}_{Y\hat{Y}}|} \quad (8)$$

Special attention is needed for fluid evaluation. For True Negative(TN) cases where both ground truth and predicted fluid are absent, the NSD score should be the correct prediction. For False Positive(FP) and False Negative(FN) cases where the fluid is only present in one of the ground truths or predicted segmentations, the NSD score should be zero as the incorrect prediction. We set τ to 10 pixels for all classes, roughly 3% of the shortest image edge. The model performance will be evaluated without any of the post-processing steps mentioned in the original papers.

Additionally, we define the Under-Segmentation Score (USS) and the Over-Segmentation Score (OSS) to evaluate if the model fails to detect certain regions or assigns excessive labels to a class. Given the confusion matrix for N classes:

$$CM = \begin{bmatrix} TP_1 & FP_{1,2} & FP_{1,3} & \dots & FP_{1,N} \\ FN_{2,1} & TP_2 & FP_{2,3} & \dots & FP_{2,N} \\ FN_{3,1} & FN_{3,2} & TP_3 & \dots & FP_{3,N} \\ \vdots & \vdots & \vdots & \ddots & \vdots \\ FN_{N,1} & FN_{N,2} & FN_{N,3} & \dots & TP_N \end{bmatrix} \quad (9)$$

We compute the USS and OSS for certain class C as:

$$USS_C = \frac{\sum_{\forall j \neq C} CM[C, j]}{\sum CM[C, :]} \quad (10)$$

$$OSS_C = \frac{\sum_{\forall i \neq C} CM[i, C]}{\sum CM[:, C]} \quad (11)$$

A higher USS score indicates that a significant portion of the ground truth class C was not detected, leading to under-segmentation, while a higher OSS score suggests that the model over-predicts class C , leading to over-segmentation.

G. Thickness Analysis

Layer thickness computation is performed using the K-Nearest Neighbors (K-NN) algorithm. The layer boundaries are converted into 3D point clouds. For each data point on the upper layer, the closest corresponding point on the lower layer is identified based on Euclidean distance. The distance is properly adjusted by the voxel dimension along each axis. The thickness maps are resized to the resolution of 350×350 for consistent representation. Due to their unbounded nature on one side, the Vitreous and Choroid layers are excluded from these calculations. Given the anatomical complexity of the foveal pit, the central region thickness is excluded from the analysis to ensure more reliable and interpretable measurements.

The thickness of fluid and hyperreflective foci (HRF) regions is computed through direct accumulation, which is subsequently projected onto an en-face view for visualization. The Early Treatment Diabetic Retinopathy Study (ETDRS) grid is employed to assess thickness variations systematically across different macular regions. As depicted in Figure 3, this grid divides the macula into three concentric circles with diameters of 1mm, 3mm, and 6mm, all centered on the fovea. These circles define the central, inner, and outer subfields, subdivided into four quadrants: superior, inferior, nasal, and temporal.

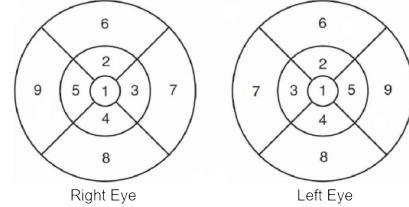


Fig. 3: ETDRS diagram for both left and right eyes. The diameters of the central circle, inner ring, and outer ring were 1 mm, 3 mm, and 6 mm, respectively. Nine subfields are numbered and named as follows: 1-CS(Central Subfield), 2-SI(Superior Inner), 3-NI(Nasal Inner), 4-II(Inferior Inner), 5-TI(Temporal Inner), 6-SO(Superior Outer), 7-NO(Nasal Outer), 8-IO(Inferior Outer), 9-TO(Temporal Outer).

III. RESULTS

A. Segmentation

Table II presents the segmentation results for four models, with values averaged across five-fold cross-validation. Tables IIa and IIb separately report the DSC and NSD metrics. A repeated-measures analysis of variance (ANOVA) is conducted to compute the F-statistics and p-values for each retinal layer in both DSC and NSD. The "Avg" column represents the average performance across all layers, with the highest score for each layer highlighted in bold.

SwinUNETR achieves the highest overall DSC and NSD among the evaluated models, demonstrating superior segmentation performance, particularly in the OPL, Choroid, and HRF regions. VM-UNet exhibits competitive performance, achieving the best DSC and NSD scores in the Vitreous, RNFL, and fluid regions. U-Net and SegFormer perform comparably, though U-Net slightly outperforms SegFormer

in DSC across most layers, whereas SegFormer demonstrates marginally better NSD performance.

Notably, high F-values and small p-values are observed in the RNFL, GCL+IPL, INL, ONL+IS, fluid, and HRF layers, indicating significant variability in segmentation accuracy across models within these regions. These findings suggest that model predictions are less consistent in these layers, potentially due to structural complexity or segmentation challenges inherent to these regions.

Figure 4 presents the mean difference in DSC and NSD between each model pair across retinal regions. For a model pair denoted as "A vs B," the mean difference is computed by subtracting model A's mean performance from model B's. The significance of these differences is indicated by an asterisk marker preceding the model pair: "****" denotes strong statistical significance ($p < 0.001$), "***" represents moderate significance ($p < 0.01$), and "**" indicates statistical significance at $p < 0.05$. The absence of a marker signifies no significant difference.

Significant mean differences with strong statistical significance are observed in the fluid and HRF regions. SwinUNETR and VM-UNet consistently demonstrate superior performance across retinal layers. While U-Net and SegFormer perform competitively in most layers, their performance in fluid and HRF regions is inferior to that of SwinUNETR and VM-UNet.

SwinUNETR and VM-UNet exhibit comparable performance in the INL, OPL, Choroid, and fluid regions for DSC. However, VM-UNet significantly outperforms SwinUNETR in the Vitreous, RNFL, GCL+IPL, and ONL+IS layers, whereas SwinUNETR achieves considerably better performance than VM-UNet in the EZ, OS, RPE, and HRF regions. Regarding NSD, SwinUNETR demonstrates a significantly larger NSD than VM-UNet in the Vitreous, OPL, ONL+IS, RPE, Choroid, and HRF layers, with no significant differences observed in the remaining regions.

Figure 5 presents examples of segmentation model predictions. Each sub-image displays five B-scans selected from the 60 central B-scans. The predicted segmentation is generated using the sub-fold model corresponding to the test set to which the patient belongs.

Figure 5a illustrates an NPDR patient exhibiting severe intraretinal fluid. All four models successfully segment the majority of fluid regions. However, U-Net and SegFormer demonstrate weaker fine-layer segmentation performance than SwinUNETR and VM-UNet, particularly in the RNFL and OPL layers. VM-UNet excels in preserving layer continuity and structural integrity, whereas U-Net and SwinUNETR exhibit discontinuities in the OPL layer in the fourth and fifth B-scans. Notably, VM-UNet tends to under-segment the fluid relative to the other models.

Figure 5b displays an NPDR patient with pronounced HRF. Shading artifacts beneath large HRF clusters disrupt the continuity of the lower layers. VM-UNet demonstrates superior performance in maintaining layer integrity despite losing pixel intensity in the bottom three B-scans. In contrast, U-Net and SegFormer struggle to compensate for these artifacts, while SwinUNETR erroneously misclassifies portions of HRF within the Choroidal region.

Figure 5c depicts a PDR patient with severe fluid accumulation. U-Net exhibits the weakest performance in fluid segmentation among all models, particularly in the third and fourth B-scans. Additionally, all models show varying degrees of under-segmentation in the final B-scan.

Figure 5d illustrates a PDR patient with partial retinal detachment. VM-UNet demonstrates robust performance across all Example B-scans, providing a more accurate segmentation of the RNFL compared to the other models.

Figure 6 shows the USS and OSS for the top-2 performance models SwinUNETR and VM-UNet. VM-UNet shows lower USS than SwinUNETR in most regions except for HRF, and it has less over-segmentation in most areas except for INL, OPL, EZ and OS. Overall, both models tend to under-segment in OPL, EZ and OS layers, plus the fluid and HRF. Over-segmentation is observed in the INL, OPL, ONL+IS, EZ and OS layers.

B. Thickness

Thickness measurements are computed from the ground-truth labels and predicted segmentation from SwinUNETR and VM-UNet. Thickness measurements are derived from both the ground-truth annotations and the segmentation predictions generated by SwinUNETR and VM-UNet. Statistical differences among these measurements are evaluated using repeated-measures ANOVA, with results detailed in Table III. The p-values of Tukey HSD are also reported if the p-value of ANOVA is less than 0.05. When comparing the ground truth with the SwinUNETR, significant thickness differences are found in the SO and IO sectors of the RPE. The significant thickness differences in the SO sector of OPL and SO, NO, and IO sectors of EZ are observed between the ground truth and VM-UNet. No statistical discrepancies are shown from the rest of the layer sectors. These findings indicate that both models are generally reliable for estimating retinal layer thicknesses across most sectors. Subsequent results in this study are based on the ground-truth segmentation.

Fig 7 shows the thickness distribution across different retinal layers and sectors for NPDR and PDR groups. The outliers are removed outside the 5th and 95th percentiles, allowing a more robust interpretation of group differences. The diamond markers in each subplot show the mean thickness of each DR group without outlier removal. The PDR group has larger mean values and broader distributions in most sectors of fluid and HRF, whereas the NPDR group has larger mean thickness in most sectors of GCL+IPL and all sectors of ONL+IS.

Statistical significance between the retinal thickness and DR groups is analyzed in Table IV. The thickness analysis is applied to the predicted segmentation of the top-2 performance models SwinUNETR and VM-UNet for comparison with the ground-truth segmentation. For each layer sector, the p-values of Welch's t-test (first row) and Analysis of Covariance (ANCOVA) adjusted by age, gender and diabetes duration (second row) are calculated. P-values less than 0.05 are considered statistically significant. For ground-truth results, PDR has a significantly larger thickness than NPDR in the SO sector of OPL. Significantly larger fluid and HRF accumulation are

Dice \ Layer \ Model	Vitreous	RNFL	GCL+IPL	INL	OPL	ONL+IS	EZ	OS	RPE	Choroid	Fluid	HRF	Avg.
U-Net	0.9887	0.8723	0.8928	0.8180	0.7714	0.9151	0.7247	0.7331	0.8510	0.9800	0.2522	0.4075	0.7672
SegFormer	0.9897	0.8722	0.8932	0.8157	0.7680	0.9139	0.7210	0.7254	0.8403	0.9772	0.2122	0.3228	0.7543
SwinUNETR	0.9871	0.8713	0.8961	0.8259	0.7788	0.9148	0.7175	0.7267	0.8440	0.9804	0.2806	0.4402	0.7719
VM-UNet	0.9899	0.8740	0.8988	0.8269	0.7768	0.9185	0.7120	0.7173	0.8396	0.9798	0.2813	0.4211	0.7697
<i>F-value</i>	18.86	161.84	95.87	50.10	37.33	58.13	14.44	13.58	13.74	5.569	33.97	52.64	-
<i>p-value</i>	4.130×10^{-5}	2.504×10^{-10}	5.322×10^{-5}	2.166×10^{-7}	1.110×10^{-6}	9.368×10^{-8}	1.545×10^{-4}	2.072×10^{-4}	1.961×10^{-4}	9.023×10^{-3}	1.861×10^{-6}	1.640×10^{-7}	-

(a) Mean Dice Similarity Coefficient (DSC) with repeated-measure ANOVA results

NSD \ Layer \ Model	Vitreous	RNFL	GCL+IPL	INL	OPL	ONL+IS	EZ	OS	RPE	Choroid	Fluid	HRF	Avg.
U-Net	0.9540	0.8860	0.8408	0.8555	0.8381	0.8414	0.9338	0.9252	0.8786	0.9160	0.2847	0.5187	0.8061
SegFormer	0.9604	0.8888	0.8455	0.8580	0.8438	0.8434	0.9343	0.9231	0.8700	0.9181	0.2253	0.4105	0.7934
SwinUNETR	0.9576	0.8890	0.8499	0.8661	0.8493	0.8497	0.9313	0.9199	0.8726	0.9207	0.3186	0.5546	0.8149
VM-UNet	0.9628	0.8899	0.8484	0.8644	0.8425	0.8452	0.9327	0.9190	0.8586	0.9167	0.3221	0.5418	0.8120
<i>F-value</i>	27.65	36.34	31.55	22.64	11.30	4.054	19.06	12.36	3.485	6.568	19.62	44.15	-
<i>p-value</i>	5.640×10^{-6}	1.288×10^{-6}	2.776×10^{-6}	1.614×10^{-5}	4.901×10^{-4}	2.632×10^{-2}	3.915×10^{-5}	3.238×10^{-4}	4.142×10^{-2}	4.864×10^{-3}	3.372×10^{-5}	4.389×10^{-7}	-

(b) Mean Normalized Surface Dice (NSD) with repeated-measure ANOVA results

TABLE II: Comparison of segmentation performance across four models. Dice and NSD scores are calculated by averaging over five validation folds. The "Average" column represents the mean performance across all regions per model. The best score in each layer is highlighted in **bold**. The bottom rows show the F-value and p-value from repeated-measures ANOVA for statistical significance.

observed in the SO sector and TO sector, respectively. ONL+IS layer thickness is significantly larger in SI, NI and TI sectors for NPDR compared to PDR. After confounders adjustment, the significance of the ONL+IS TI sector and HRF TO sector vanishes.

Figure 8 presents four examples of thickness comparisons between NPDR and PDR groups using the ETDRS diagram described in Figure 3. Each example shows four regions that are reported with significant thickness differences in Table IV. Figures 8a–8d correspond to cases of a 57-year-old male OD, a 54-year-old male OS, and a 59-year-old female OD and OS images, respectively. Each pair of patients is matched by age, gender, and eye laterality. For each retinal region, the first row displays the En Face image overlaid with the corresponding layer thickness heatmap, while the second row presents the sector-wise quantitative average thickness. The En Face image is generated using each layer’s maximum intensity projection (MIP). For fluid and HRF, the En Face projection is derived from the entire retinal body (from the ILM to the BM), with thickness representing the accumulated volume in μm^3 . From these figures 8a–8d, PDR exhibits a larger thickness than NPDR in nearly all OPL sectors. Conversely, the inner sectors of ONL+IS are significantly smaller for PDR. PDR has a larger and broader distribution of fluid and HRF accumulation in most sectors than NPDR. The findings are consistent with previous results.

We also evaluated the association between retinal layer sector thickness and visual acuity, as shown in table V. The evaluation is performed for NPDR and PDR separately. Each value represents the Pearson correlation coefficient with a p-value within a specific layer sector. The p-values are adjusted by age, gender and diabetes duration. For NPDR, significant positive correlations are found in the SO sector of ONL+IS, the IO sector of RPE, the SO sector of fluid and the SI plus SO sectors of HRF. For PDR, we observe significant positive correlations in the NO sector of EZ, IO sector of OS, and

NO sector of fluid. This finding indicates that thickening these layers and accumulations of fluid and HRF may result in worse vision.

DISCUSSION

The segmentation performance varied across models, highlighting differences in architectural strengths and their ability to segment specific retinal layers and fluid-related abnormalities. SwinUNETR and VM-UNet consistently achieved high DSC and NSD scores, indicating their robustness in handling complex retinal structures. SwinUNETR particularly excelled in segmenting the OPL and HRF layers, which may be attributed to its transformer-based architecture that effectively captures long-range dependencies. VM-UNet, on the other hand, performed better in segmenting the fluid regions, suggesting that its sequential nature enhances segmentation continuity, particularly in areas with less distinct boundaries.

The performance differences in DSC and NSD indicate that while both models perform well, their strengths lie in different layers. DSC reflects volumetric segmentation accuracy, whereas SwinUNETR demonstrated better performance in HRF, likely due to its ability to differentiate small scattered hyper-reflective lesions. However, NSD provides insights into surface delineation accuracy, where VM-UNet showed superior performance in fluid regions, maintaining smoother boundaries compared to other models. U-Net and SegFormer, though competitive in some layers, exhibited weaker performance in fine layer segmentation, particularly in RNFL and OPL, where structural continuity is essential for accurate disease characterization. Although the SwinUNETR slightly outperforms VM-UNet in several regions, VM-UNet has significantly lower computational complexity ($O(N)$) than SwinUNETR ($O(N^2)$), which is crucial for remote deployment in clinics with limited computational resources.

The segmentation of fluid and HRF remains a significant challenge across all models. Fluid regions exhibit substantial

Region	Sector							
	SI	NI	II	TI	SO	NO	IO	TO
RNFL	0.127	0.820	0.519	0.493	0.001	0.557	0.019	0.767
	-	-	-	-	0.565 / 0.609	-	0.566 / 0.674	-
GCL+IPL	0.132	0.630	0.649	0.801	0.076	0.239	0.108	0.620
	-	-	-	-	-	-	-	-
INL	0.108	0.001	0.005	0.055	0.000	0.042	0.003	0.000
	-	0.557 / 0.093	0.870 / 0.205	-	0.562 / 0.324	0.677 / 0.474	0.818 / 0.445	0.517 / 0.561
OPL	0.002	0.018	0.106	0.005	0.000	0.034	0.039	0.001
	0.992 / 0.319	0.860 / 0.594	-	0.870 / 0.558	0.553 / 0.045	0.869 / 0.542	0.978 / 0.503	0.997 / 0.341
ONL+IS	0.789	0.059	0.085	0.039	0.065	0.889	0.014	0.403
	-	-	-	0.543 / 0.620	-	-	0.795 / 0.983	-
EZ	0.015	0.250	0.011	0.365	0.000	0.000	0.000	0.101
	0.211 / 0.111	-	0.773 / 0.318	-	0.169 / 0.000	0.430 / 0.003	0.282 / 0.000	-
OS	0.214	0.001	0.182	0.530	0.062	0.127	0.028	0.190
	-	0.069 / 0.431	-	-	-	-	0.460 / 0.503	-
RPE	0.321	0.001	0.002	0.366	0.001	0.019	0.000	0.368
	-	0.092 / 1.000	0.174 / 0.885	-	0.024 / 0.970	0.184 / 0.677	0.001 / 0.460	-
Fluid	0.109	0.114	0.399	0.044	0.005	0.073	0.041	0.515
	-	-	-	0.944 / 0.997	0.089 / 0.803	-	0.197 / 0.998	-
HRF	0.093	0.112	0.002	0.038	0.000	0.000	0.002	0.011
	-	-	0.978 / 0.457	0.731 / 0.410	0.858 / 0.460	0.818 / 0.344	0.999 / 0.613	0.999 / 0.812

TABLE III: Statistical comparison of retinal layer thickness between ground truth and two segmentation models (SwinUNETR and VM-UNet) across retinal layers and sectors. The first p-value per layer is from repeated-measures ANOVA (three groups). Subsequent p-values are from Tukey HSD pairwise comparisons (Ground-truth vs. SwinUNETR, Ground-truth vs. VM-UNet), reported only if ANOVA $p < 0.05$. Significant p-values < 0.05 are in **bold**.

variability, with VM-UNet demonstrating better spatial continuity but often under-segmenting these regions. In contrast, SwinUNETR captures fluid regions more extensively but is prone to occasional over-segmentation. HRF segmentation presents an even more significant challenge due to the presence of small, widely distributed hyper-reflective regions. Both models tend to under-segment fluid and HRF, frequently misclassifying them into adjacent retinal layers such as OPL and ONL+IS. Moreover, SwinUNETR generally exhibits a greater tendency to under-segment retinal regions than VM-UNet. Although significant weight adjustments were applied to fluid and HRF regions, as described in Section II-E, additional strategies are needed to enhance model learning and improve segmentation performance in these complex regions.

The accuracy of the predicted segmentation is further assessed through thickness calculations. Both SwinUNETR and VM-UNet yield comparable thickness measurements with minimal variations across layer sectors. In the context of this cohort study, SwinUNETR emerges as the preferred choice, as the deviations observed in the RPE do not compromise the statistical significance presented in Table IV. In contrast, the notable bias in the SO sector of the OPL exhibited by VM-UNet could undermine the reliability of its reported significance.

Significant differences in retinal layer thickness between

NPDR and PDR offer valuable insights into the progression of DR. Prior to adjusting for potential confounders, including age, gender, and duration of diabetes, OPL was significantly thicker in the SO sector for PDR. It suggests that possible fluid leakage of OPL barrier breakdown due to hypoxia is more prominent in PDR patients. After adjusting for confounders, statistical significance persists, suggesting that this structural change alone may serve as a potential biomarker for the early detection of PDR. ONL+IS exhibited significant thinning in PDR in the SI, NI, and TI sectors before adjustment, reflecting the photoreceptor degeneration and apoptosis due to potential neurodegeneration and inflammatory responses. However, after adjusting for confounders, the TI sector is no longer significant, suggesting that systemic factors play a role in some but not all aspects of ONL+IS thinning in PDR.

Fluid accumulation was significantly more prevalent in PDR than NPDR in the SO sector. This suggests that while variability in fluid distribution may limit statistical significance, extensive fluid in PDR remains clinically relevant. The increased fluid volume aligns with the pathological features of PDR, where extensive vascular leakages lead to blood-retina barrier breakdown and, eventually, fluid accumulation. Before adjustment, HRF was significantly more widespread in NPDR than PDR, particularly in the II and SO sectors, supporting the hypothesis that HRF is an early marker of inflammation. How-

Region	Sector							
	SI	NI	II	TI	SO	NO	IO	TO
RNFL	0.578	0.320	0.418	0.321	0.837	0.776	0.838	0.087
	0.524	0.556	0.962	0.183	0.833	0.846	0.940	0.075
GCL+IPL	0.125	0.058	0.568	0.097	0.796	0.924	0.920	0.173
	0.390	0.390	0.979	0.242	0.530	0.284	0.645	0.530
INL	0.853	0.585	0.232	0.228	0.475	0.838	0.933	0.963
	0.872	0.958	0.543	0.263	0.299	0.713	0.706	0.561
OPL	0.499	0.675	0.881	0.997	0.037	0.679	0.710	0.578
	0.315	0.620	0.844	0.769	0.016	0.394	0.575	0.341
ONL+IS	0.010	0.005	0.254	0.034	0.148	0.069	0.296	0.201
	0.033	0.023	0.476	0.082	0.240	0.293	0.607	0.586
EZ	0.368	0.937	0.343	0.955	0.987	0.928	0.633	0.699
	0.610	0.550	0.130	0.696	0.846	0.807	0.575	0.613
OS	0.620	0.966	0.985	0.694	0.835	0.942	0.927	0.868
	0.572	0.990	0.919	0.826	0.764	0.935	0.827	0.756
RPE	0.785	0.292	0.889	0.990	0.119	0.774	0.583	0.351
	0.818	0.580	0.824	0.901	0.141	0.660	0.342	0.663
Fluid	0.513	0.127	0.493	0.618	0.014	0.886	0.791	0.790
	0.526	0.128	0.574	0.610	0.031	0.937	0.792	0.921
HRF	0.644	0.059	0.612	0.159	0.361	0.365	0.603	0.049
	0.685	0.079	0.346	0.240	0.356	0.383	0.510	0.118

TABLE IV: Statistical significance of retinal thickness plus fluid and HRF volume differences for NPDR vs PDR. Each cell of two p-values is derived from the ground-truth segmentation. Within each layer, the value on the first row represents the p-value from Welch’s t-test, and the second row represents the p-values adjusted by age, gender and duration of diabetes using Analysis of Covariance (ANCOVA). The p-values less than 0.05 are highlighted in **bold**.

ever, this does not necessarily signify reduced disease severity of PDR but rather a transition to neovascularization toward deeper retinal layers. The chronic vascular leakage may cause the HRF to disperse or form into larger hard exudates and hemorrhages with less visibility in OCT. After adjusting for confounders, these differences lost statistical significance. This suggests that while HRF may be an important early indicator of neuroinflammation, its distribution may be influenced by demographic and disease-specific factors.

Our findings reveal significant associations between retinal layer thickness and visual acuity within NPDR and PDR patients. In NPDR, layer thickening of ONL+IS and RPE plus the fluid and HRF accumulation in several sectors are significantly correlated with worse vision. It implies that possible microvascular leakage and inflammation in these regions result in vision degradation. When progressing to PDR, chronic ischemia and neovascularization-related pathologies are reflected by the significant thickening of EZ and OS layers. Severe fluid accumulation in the NO sector distorts the retinal structural functionalities, leading to diminished vision. Therefore, proper early intervention during the NPDR stage is crucial to prevent irreversible retinal damage.

IV. LIMITATION AND FUTURE WORK

Despite the strengths of this study, several limitations must be acknowledged.

First, manual labelling imperfections impact both model performance and thickness measurements. Retinal layer segmentation is inherently challenging due to subtle boundary variations and overlapping structures. In cases where excessive fluid penetrates the layer boundaries, some portions of the layer become invisible or physically diminished. More clinical expertise is needed to segment the extreme instances properly. HRF segmentation suffers from inconsistencies in ground-truth annotations, as small, widely distributed foci are challenging to delineate manually. Interestingly, in some cases, automated models provided more precise segmentations than the ground-truth labels. For example, for the first B-scan in Figure 5a, the predictions of SegFormer and SwinUNETR have better RNFL segmentation than the ground truth with a smoother and more precise layer boundary. For the first B-scan in Figure 5c, no fluid is manually annotated, but the segmentation models, except for SegFormer, predict potential intra-retinal fluid across the OPL and ONL+IS regions. Additionally, using more pre-processing and post-processing techniques may help improve the performance, such as the pixel-wise relative positional map as an extra input and random forest classifier as a label refiner (Ma et al., 2021).

Second, additional model comparisons may be necessary to provide a more comprehensive evaluation of segmentation approaches. While SwinUNETR and VM-UNet demonstrated superior performance, other architectures excel in certain per-

Region	Sector							
	SI	NI	II	TI	SO	NO	IO	TO
Non-Proliferative Diabetic Retinopathy (NPDR)								
RNFL	0.220 (0.084)	0.215 (0.091)	0.080 (0.533)	0.120 (0.348)	0.199 (0.119)	0.112 (0.384)	0.195 (0.126)	-0.004 (0.974)
GCL+IPL	-0.033 (0.798)	-0.038 (0.765)	-0.076 (0.553)	-0.133 (0.299)	0.053 (0.680)	-0.063 (0.623)	0.077 (0.547)	0.007 (0.959)
INL	-0.108 (0.398)	-0.154 (0.227)	-0.175 (0.171)	-0.146 (0.254)	0.127 (0.322)	-0.011 (0.932)	-0.108 (0.398)	0.011 (0.934)
OPL	0.126 (0.324)	0.043 (0.740)	0.118 (0.358)	0.049 (0.703)	0.213 (0.093)	0.058 (0.651)	0.106 (0.408)	0.118 (0.356)
ONL+IS	0.002 (0.986)	-0.098 (0.447)	0.055 (0.666)	-0.006 (0.962)	0.284 (0.024)	0.077 (0.547)	0.184 (0.148)	0.172 (0.178)
EZ	0.010 (0.940)	-0.033 (0.800)	-0.013 (0.921)	0.075 (0.561)	0.017 (0.896)	-0.044 (0.734)	-0.085 (0.506)	0.026 (0.841)
OS	0.111 (0.386)	-0.152 (0.235)	0.015 (0.905)	0.016 (0.898)	0.125 (0.331)	-0.045 (0.729)	-0.022 (0.865)	0.008 (0.952)
RPE	0.018 (0.890)	0.011 (0.929)	0.128 (0.316)	0.016 (0.902)	0.051 (0.690)	-0.045 (0.727)	0.271 (0.032)	0.216 (0.089)
Fluid	0.150 (0.242)	0.140 (0.275)	0.225 (0.076)	0.212 (0.095)	0.256 (0.043)	0.118 (0.359)	0.196 (0.124)	0.145 (0.258)
HRF	0.278 (0.028)	0.159 (0.213)	0.048 (0.707)	0.107 (0.405)	0.311 (0.013)	0.176 (0.167)	0.109 (0.394)	-0.001 (0.992)
Proliferative Diabetic Retinopathy (PDR)								
RNFL	0.059 (0.696)	0.114 (0.443)	0.020 (0.892)	0.070 (0.640)	0.075 (0.615)	0.087 (0.559)	0.014 (0.927)	-0.047 (0.755)
GCL+IPL	-0.068 (0.652)	-0.053 (0.723)	-0.131 (0.378)	-0.031 (0.838)	-0.248 (0.093)	-0.119 (0.427)	-0.201 (0.176)	-0.004 (0.979)
INL	0.011 (0.941)	0.000 (0.998)	-0.152 (0.309)	-0.155 (0.298)	-0.044 (0.769)	0.121 (0.418)	-0.091 (0.543)	-0.168 (0.258)
OPL	0.084 (0.575)	-0.096 (0.522)	-0.103 (0.489)	-0.019 (0.902)	0.006 (0.970)	0.072 (0.630)	-0.073 (0.625)	-0.129 (0.388)
ONL+IS	-0.038 (0.800)	0.007 (0.961)	0.062 (0.681)	-0.003 (0.982)	0.112 (0.454)	0.170 (0.254)	0.111 (0.459)	0.095 (0.525)
EZ	0.163 (0.274)	0.280 (0.057)	0.185 (0.214)	0.069 (0.647)	0.025 (0.870)	0.290 (0.048)	0.148 (0.321)	0.263 (0.074)
OS	0.212 (0.153)	0.137 (0.359)	0.022 (0.883)	0.202 (0.174)	0.214 (0.148)	0.251 (0.089)	0.359 (0.013)	0.257 (0.081)
RPE	0.020 (0.891)	0.005 (0.971)	-0.057 (0.704)	0.106 (0.480)	0.168 (0.258)	0.097 (0.515)	0.132 (0.377)	0.194 (0.191)
Fluid	-0.011 (0.940)	0.150 (0.315)	0.169 (0.256)	-0.003 (0.982)	0.215 (0.147)	0.359 (0.013)	0.056 (0.710)	-0.165 (0.267)
HRF	-0.071 (0.638)	0.087 (0.562)	-0.002 (0.989)	-0.115 (0.442)	-0.013 (0.930)	0.112 (0.453)	-0.109 (0.468)	-0.230 (0.120)

TABLE V: Partial correlation between retinal layer thickness and visual acuity in logMAR for NPDR and PDR. Each cell presents the Pearson correlation coefficient (p-value) adjusted by age, gender, and diabetes duration. Statistically significant values ($p < 0.05$) are highlighted in **bold**.

spectives. For example, MedSAM enables universal medical image segmentation with zero-shot capabilities (Ma et al., 2023). The self-supervised few-shot semantic segmentation can be used for a limited number of labels (Ouyang et al., 2022). A broader comparison across multiple deep learning models could offer more insights into the trade-offs between performance, efficiency, and generalizability.

Third, this study’s cross-sectional nature limits its ability to track disease progression over time. Longitudinal studies would provide better insights into how retinal layer thickness evolves in DR. For example, several studies report RNFL/GCL thinning during progression of DR, which has become one of the most important preclinical biomarkers for DR severity evaluation (Bhaskaran et al., 2023) (Oshitari et al., 2009) (Park et al., 2011). Additionally, while the sample size is sufficient to detect significant differences, it may limit the generalizability of the findings. A larger dataset encompassing a broader range of DR severities and treatment histories could provide more robust conclusions. In our study, no significant RNFL thickness difference is found between the NPDR and PDR groups. Fig 7 show explicit GCL+IPL thinning of PDR in terms of the mean and interquartile range, but only the NI sector exhibits marginal significance ($p = 0.058$). Expanding the cohort to include more diverse patient populations may help improve the applicability of the findings across different clinical settings.

Fourth, the lack of a detailed NPDR severity grading system may limit the ability to distinguish early, intermediate, and severe NPDR stages. Different NPDR severities likely exhibit distinct retinal layer changes, and a more granular

classification system could enhance the understanding of DR progression. Future studies should explore integrating severity-based stratification to assess how thickness variations differ across NPDR subtypes. To our best knowledge, most DR grading datasets with public access focus on fundus color images like Messidor³ and DRTiD⁴. Additional efforts are needed to investigate the OCT image associated with DR severity levels, which are precisely determined using corresponding fundus images.

Lastly, integrating multi-modal imaging techniques such as OCT angiography (OCTA) could provide additional insights into the vascular changes associated with DR. For example, Alam *et al.* discovered the difference of vascular complexity features between NPDR and PDR patients (Alam et al., 2021). Multiple OCT parameters are significantly correlated with DR severity (Laotaweerungsawat et al., 2020). Combining structural OCT findings with functional vascular imaging may improve disease characterization and facilitate more targeted therapeutic interventions.

V. CONCLUSION

This study highlights the strengths and limitations of current segmentation models in analyzing DR-related structural changes. SwinUNETR and VM-UNet demonstrate strong performance, particularly in segmenting complex retinal layers and fluid regions, but challenges remain in HRF segmentation due to its small and widely distributed nature. The analysis of

³<https://www.adcis.net/en/third-party/messidor/>

⁴<https://github.com/FDU-VTS/DRTiD>

retinal layer thickness differences between NPDR and PDR reveals distinct structural alterations, with significant findings in OPL, ONL+IS, fluid, and HRF distributions. The different responses of visual acuity within NPDR and PDR suggest a progression from adaptive retinal changes in NPDR to pathological neurodegeneration and edema-driven impairment in PDR, reinforcing the need for early intervention to prevent irreversible vision loss.

These results emphasize the potential for deep-learning models to improve disease monitoring and classification, and they provide valuable insights into the progressive nature of retinal changes in DR. However, addressing limitations such as manual labelling inconsistencies, cross-sectional study constraints, and limited NPDR severity stratification will be critical in refining segmentation algorithms and advancing the clinical utility of automated OCT analysis. Future efforts should focus on integrating longitudinal data, expanding datasets, and incorporating multi-modal imaging to enhance the predictive power of segmentation-based disease assessment tools.

VI. FUNDING AND ACKNOWLEDGEMENT

We would like to thank Roy Boustani, Talha Mohammed and Shuting Xing for their help with manual segmentation and corrections. This study was funded by the National Sciences and Engineering Research Council of Canada; Canadian Institutes of Health Research, Compute Canada, and Wake Forest University School of Medicine Startup Funding. The sponsor or funding organization had no role in the design or conduct of this research. The pipelines developed in this work will be available in our Cloud Engine Resource for Accelerated Medical Image Computing for Clinical Applications (CERAMICCA) platform (<https://ceramicca.from-ca.com/>).

VII. DECLARATION OF COMPETING INTEREST

All co-authors declare no conflict of interest.

REFERENCES

- Minhaj Alam, David Le, Jennifer I. Lim, and Xincheng Yao. VASCULAR COMPLEXITY ANALYSIS IN OPTICAL COHERENCE TOMOGRAPHY ANGIOGRAPHY OF DIABETIC RETINOPATHY. *Retina*, 41(3):538–545, 3 2021. ISSN 0275-004X. doi: 10.1097/IAE.0000000000002874.
- Aparna Bhaskaran, Mahesh Babu, N A Sudhakar, Krishna Prasad Kudlu, and B C Shashidhara. Study of retinal nerve fiber layer thickness in diabetic patients using optical coherence tomography. *Indian Journal of Ophthalmology*, 71(3):920–926, 3 2023. ISSN 0301-4738. doi: 10.4103/ijo.IJO_1918_22. URL https://journals.lww.com/10.4103/ijo.IJO_1918_22.
- David J. Browning, Christina M. Fraser, and Stephen Clark. The Relationship of Macular Thickness to Clinically Graded Diabetic Retinopathy Severity in Eyes without Clinically Detected Diabetic Macular Edema. *Ophthalmology*, 115(3): 533–539, 3 2008. ISSN 01616420. doi: 10.1016/j.ophtha.2007.06.042.
- Di Cao, Di Yang, Zhaoxin Huang, Yixiong Zeng, Guanghui Chen, Zhaohui Wang, and Ke Wu. The Prevalence of Diabetic Retinopathy in Smokers: A Meta-Analysis. *PLoS ONE*, 12(4):e0175800, 2017. doi: 10.1371/journal.pone.0175800. URL <https://journals.plos.org/plosone/article?id=10.1371/journal.pone.0175800>.
- Ning Cheung, Paul Mitchell, and Tien Y Wong. Diabetic Retinopathy. *The Lancet*, 376(9735):124–136, 2016. doi: 10.1016/S0140-6736(09)62124-3. URL [https://www.thelancet.com/journals/lancet/article/PIIS0140-6736\(09\)62124-3/fulltext](https://www.thelancet.com/journals/lancet/article/PIIS0140-6736(09)62124-3/fulltext).
- Stephanie J Chiu, Xiao T Li, Peter Nicholas, Cynthia A Toth, Joseph A Izatt, and Sina Farsiu. Automatic segmentation of seven retinal layers in SDOCT images congruent with expert manual segmentation. *Opt. Express*, 18(18):19413–19428, 8 2010. doi: 10.1364/OE.18.019413. URL <https://opg.optica.org/oe/abstract.cfm?URI=oe-18-18-19413>.
- Hee Yoon Cho, Dong Hoon Lee, Song Ee Chung, and Se Woong Kang. Diabetic Retinopathy and Peripapillary Retinal Thickness. *Korean Journal of Ophthalmology*, 24(1):16, 2010. ISSN 1011-8942. doi: 10.3341/kjo.2010.24.1.16.
- Gabriele E. Lang. Optical Coherence Tomography Findings in Diabetic Retinopathy. In *Developments in Ophthalmology*, volume 39, pages 31–47. 2007.
- A. Gonzalez, B. Remeseiro, M. Ortega, M. G. Penedo, and P. Charlon. Automatic cyst detection in OCT retinal images combining region flooding and texture analysis. In *Proceedings of the 26th IEEE International Symposium on Computer-Based Medical Systems*, pages 397–400. IEEE, 6 2013. ISBN 978-1-4799-1053-3. doi: 10.1109/CBMS.2013.6627825.
- Ali Hatamizadeh, Vishwesh Nath, Yucheng Tang, Dong Yang, Holger Roth, and Daguang Xu. Swin UNETR: Swin Transformers for Semantic Segmentation of Brain Tumors in MRI Images. 1 2022.
- Artemas Herzog, Kim L. Boyer, and Cynthia Roberts. Robust Extraction of the Optic Nerve Head in Optical Coherence Tomography. pages 395–407. 2004. doi: 10.1007/978-3-540-27816-0_34. URL http://link.springer.com/10.1007/978-3-540-27816-0_34.
- Kai Hu, Binwei Shen, Yuan Zhang, Chunhong Cao, Fen Xiao, and Xieping Gao. Automatic segmentation of retinal layer boundaries in OCT images using multiscale convolutional neural network and graph search. *Neurocomputing*, 365: 302–313, 11 2019. ISSN 09252312. doi: 10.1016/j.neucom.2019.07.079.
- Jee Taek Kim, Dong Hoon Lee, Soo Geun Joe, June-Gone Kim, and Young Hee Yoon. Changes in Choroidal Thickness in Relation to the Severity of Retinopathy and Macular Edema in Type 2 Diabetic Patients. *Investigative Ophthalmology & Visual Science*, 54(5):3378, 5 2013. ISSN 1552-5783. doi: 10.1167/iovs.12-11503.
- Barbara Eden Kobrin Klein. Overview of Epidemiologic Studies of Diabetic Retinopathy. *Ophthalmic Epidemiology*, 14(4):179–183, 2007. doi: 10.1080/09286580701396720.
- Ronald Klein, Barbara E K Klein, Scot E Moss, and Karen J Cruickshanks. The Wisconsin Epidemiologic Study of

- Diabetic Retinopathy: XXII. The twenty-five-year progression of retinopathy in persons with type 1 diabetes. *Ophthalmology*, 121(10):1992–1999, 2014. doi: 10.1016/j.ophtha.2014.03.019. URL [https://www.aaojournal.org/article/S0161-6420\(14\)00265-6/fulltext](https://www.aaojournal.org/article/S0161-6420(14)00265-6/fulltext).
- Jason Kugelman, David Alonso-Caneiro, Scott A. Read, Stephen J. Vincent, and Michael J. Collins. Automatic segmentation of OCT retinal boundaries using recurrent neural networks and graph search. *Biomedical Optics Express*, 9(11):5759, 11 2018. ISSN 2156-7085. doi: 10.1364/BOE.9.005759.
- Mikhail Kulyabin, Aleksei Zhdanov, Andrey Pershin, Gleb Sokolov, Anastasia Nikiforova, Mikhail Ronkin, Vasilii Borisov, and Andreas Maier. Segment Anything in Optical Coherence Tomography: SAM 2 for Volumetric Segmentation of Retinal Biomarkers. *Bioengineering*, 11(9):940, 9 2024. ISSN 2306-5354. doi: 10.3390/bioengineering11090940.
- Sawarin Laotaweerungsawat, Catherine Psaras, Xiuyun Liu, and Jay M. Stewart. OCT Angiography Assessment of Retinal Microvascular Changes in Diabetic Eyes in an Urban Safety-Net Hospital. *Ophthalmology Retina*, 4(4):425–432, 4 2020. ISSN 24686530. doi: 10.1016/j.oret.2019.11.008.
- Xiaoming Liu, Tianyu Fu, Zhifang Pan, Dong Liu, Wei Hu, Jun Liu, and Kai Zhang. Automated Layer Segmentation of Retinal Optical Coherence Tomography Images Using a Deep Feature Enhanced Structured Random Forests Classifier. *IEEE Journal of Biomedical and Health Informatics*, 23(4):1404–1416, 7 2019. ISSN 2168-2194. doi: 10.1109/JBHI.2018.2856276.
- Yue Liu, Yunjie Tian, Yuzhong Zhao, Hongtian Yu, Lingxi Xie, Yaowei Wang, Qixiang Ye, Jianbin Jiao, and Yunfan Liu. VMamba: Visual State Space Model. 1 2024. URL <http://arxiv.org/abs/2401.10166>.
- Da Ma, Donghuan Lu, Shuo Chen, Morgan Heisler, Setareh Dabiri, Sieun Lee, Hyunwoo Lee, Gavin Weiguang Ding, Marinko V. Sarunic, and Mirza Faisal Beg. LF-UNet – A novel anatomical-aware dual-branch cascaded deep neural network for segmentation of retinal layers and fluid from optical coherence tomography images. *Computerized Medical Imaging and Graphics*, 94:101988, 12 2021. ISSN 08956111. doi: 10.1016/j.compmedimag.2021.101988.
- Jun Ma, Yuting He, Feifei Li, Lin Han, Chenyu You, and Bo Wang. Segment Anything in Medical Images. 4 2023. doi: 10.1038/s41467-024-44824-z.
- Takeshi Mori, Kei Hanai, Yuki Yamamoto, and Naoki Yoshida. Association of diabetic retinopathy with kidney disease progression according to baseline kidney function and albuminuria status in individuals with type 2 diabetes. *Clinical and Experimental Nephrology*, 28(3):143–151, 2024. doi: 10.1007/s10157-024-02599-z. URL <https://link.springer.com/article/10.1007/s10157-024-02599-z>.
- Stanislav Nikolov, Sam Blackwell, Alexei Zverovitch, Ruheena Mendes, Michelle Livne, Jeffrey De Fauw, Yojan Patel, Clemens Meyer, Harry Askham, Bernardino Romera-Paredes, Christopher Kelly, Alan Karthikesalingam, Carlton Chu, Dawn Carnell, Cheng Boon, Derek D’Souza, Syed Ali Moinuddin, Bethany Garie, Yasmin McQuinlan, Sarah Ireland, Kiarna Hampton, Krystle Fuller, Hugh Montgomery, Geraint Rees, Mustafa Suleyman, Trevor Back, Cian Hughes, Joseph R. Ledsam, and Olaf Ronneberger. Deep learning to achieve clinically applicable segmentation of head and neck anatomy for radiotherapy. 9 2018.
- T Oshitari, K Hanawa, and E Adachi-Usami. Changes of macular and RNFL thicknesses measured by Stratus OCT in patients with early stage diabetes. *Eye (London, England)*, 23(4):884–9, 4 2009. ISSN 1476-5454. doi: 10.1038/eye.2008.119.
- Cheng Ouyang, Carlo Biffi, Chen Chen, Turkay Kart, Huaqi Qiu, and Daniel Rueckert. Self-Supervised Learning for Few-Shot Medical Image Segmentation. *IEEE Transactions on Medical Imaging*, 41(7):1837–1848, 7 2022. ISSN 0278-0062. doi: 10.1109/TMI.2022.3150682.
- Hae Young-Lopilly Park, In Tae Kim, and Chan Kee Park. Early diabetic changes in the nerve fibre layer at the macula detected by spectral domain optical coherence tomography. *The British journal of ophthalmology*, 95(9):1223–8, 9 2011. ISSN 1468-2079. doi: 10.1136/bjo.2010.191841.
- Olaf Ronneberger, Philipp Fischer, and Thomas Brox. U-Net: Convolutional Networks for Biomedical Image Segmentation. pages 234–241. 2015. doi: 10.1007/978-3-319-24574-4_{_}28.
- Abhijit Guha Roy, Sailesh Conjeti, Sri Phani Krishna Karri, Debdoot Sheet, Amin Katouzian, Christian Wachinger, and Nassir Navab. ReLayNet: retinal layer and fluid segmentation of macular optical coherence tomography using fully convolutional networks. *Biomedical Optics Express*, 8(8):3627, 8 2017. ISSN 2156-7085. doi: 10.1364/BOE.8.003627.
- Jiacheng Ruan, Jincheng Li, and Suncheng Xiang. VM-UNet: Vision Mamba UNet for Medical Image Segmentation. 2 2024.
- Santos T, Reste-Ferreira D, Marques I, Ribeiro L, Mendes L, Santos A.R., Figueira J, Lobo C, and Cunha-Vaz J. Vision Loss in Diabetic Macular Edema Is Associated with Abnormal Fluid Accumulation in the Outer Segment Layer. *Investigative Ophthalmology & Visual Science*, 65(4):153–153, 2024.
- Thomas Schlegl, Hrvoje Bogunovic, Sophie Klimescha, Philipp Seeböck, Amir Sadeghipour, Bianca Gerendas, Sebastian M. Waldstein, Georg Langs, and Ursula Schmidt-Erfurth. Fully Automated Segmentation of Hyperreflective Foci in Optical Coherence Tomography Images. 5 2018.
- Ruwan Tennakoon, Amirali K. Gostar, Reza Hoseinnezhad, and Alireza Bab-Hadiashar. Retinal fluid segmentation in OCT images using adversarial loss based convolutional neural networks. In *2018 IEEE 15th International Symposium on Biomedical Imaging (ISBI 2018)*, pages 1436–1440. IEEE, 4 2018. ISBN 978-1-5386-3636-7. doi: 10.1109/ISBI.2018.8363842.
- Zhen Ling Teo, Yih Chung Tham, Marco Yu, Miao Li Chee, Tyler Hyungtaek Rim, Ning Cheung, Mukharram M Bikbov, Ya Xing Wang, Yating Tang, Yi Lu, Ian Y Wong, Daniel Shu Wei Ting, Gavin Siew Wei Tan, Jost B Jonas, Charumathi Sabanayagam, Tien Yin Wong, and Ching Yu Cheng. Global Prevalence of Diabetic Retinopathy and Projection

- of Burden through 2045: Systematic Review and Meta-analysis. *Ophthalmology*, 128(11):1580–1591, 1 2021. ISSN 0161-6420. doi: 10.1016/J.OPHTHA.2021.04.027.
- Chuang Wang, Yaxing Wang, Djibril Kaba, Haogang Zhu, You Lv, Zidong Wang, Xiaohui Liu, and Yongmin Li. Segmentation of Intra-retinal Layers in 3D Optic Nerve Head Images. pages 321–332. 2015. doi: 10.1007/978-3-319-21969-1{_}28.
- Ho-yin Wong, Ricky Ahmat, Benny Chung-ying Zee, Simon Chun-wa Luk, Gladys Lai-ying Cheing, and Andrew Kwok-cheung Lam. Comparison of macular thickness in diabetic patients acquired from optical coherence tomography mode and optical coherence tomography angiography mode in Cirrus HD-OCT 5000. *Journal of Optometry*, 17(4):100519, 10 2024. ISSN 18884296. doi: 10.1016/j.optom.2024.100519.
- Enze Xie, Wenhai Wang, Zhiding Yu, Anima Anandkumar, Jose M. Alvarez, and Ping Luo. SegFormer: Simple and Efficient Design for Semantic Segmentation with Transformers. 5 2021.
- Xinjian Chen, M. Niemeijer, Li Zhang, Kyungmoo Lee, M. D. Abramoff, and M. Sonka. Three-Dimensional Segmentation of Fluid-Associated Abnormalities in Retinal OCT: Probability Constrained Graph-Search-Graph-Cut. *IEEE Transactions on Medical Imaging*, 31(8):1521–1531, 8 2012. ISSN 0278-0062. doi: 10.1109/TMI.2012.2191302.
- Xiaozhong Xue and Weiwei Du. Retinal Fluid Segmentation from OCT B-Scan Using Swin-Unet. In *2024 2nd International Conference on Computer Graphics and Image Processing (CGIP)*, pages 1–6. IEEE, 1 2024. ISBN 979-8-3503-7418-6. doi: 10.1109/CGIP62525.2024.00011.
- Jian Zhang, Zheng Luo, Rui Zhang, and Jing Wang. Association between sensitivity to thyroid hormone indices and type 2 diabetic microvascular complications in euthyroid patients. *Scientific Reports*, 14(1):201–211, 2024. doi: 10.1038/s41598-024-82028-z. URL <https://www.nature.com/articles/s41598-024-82028-z>.
- Ying Zhou, Ling Song, Xiaomin Yin, Wen Zhu, and Ming Zeng. Coffee intake, plasma caffeine levels, and diabetic microvascular complications: a Mendelian randomization study. *Nutrition, Metabolism and Cardiovascular Diseases*, 35(1):18–27, 2025. doi: 10.1016/j.numecd.2024.09.001. URL <https://www.sciencedirect.com/science/article/pii/S0939475325000109>.

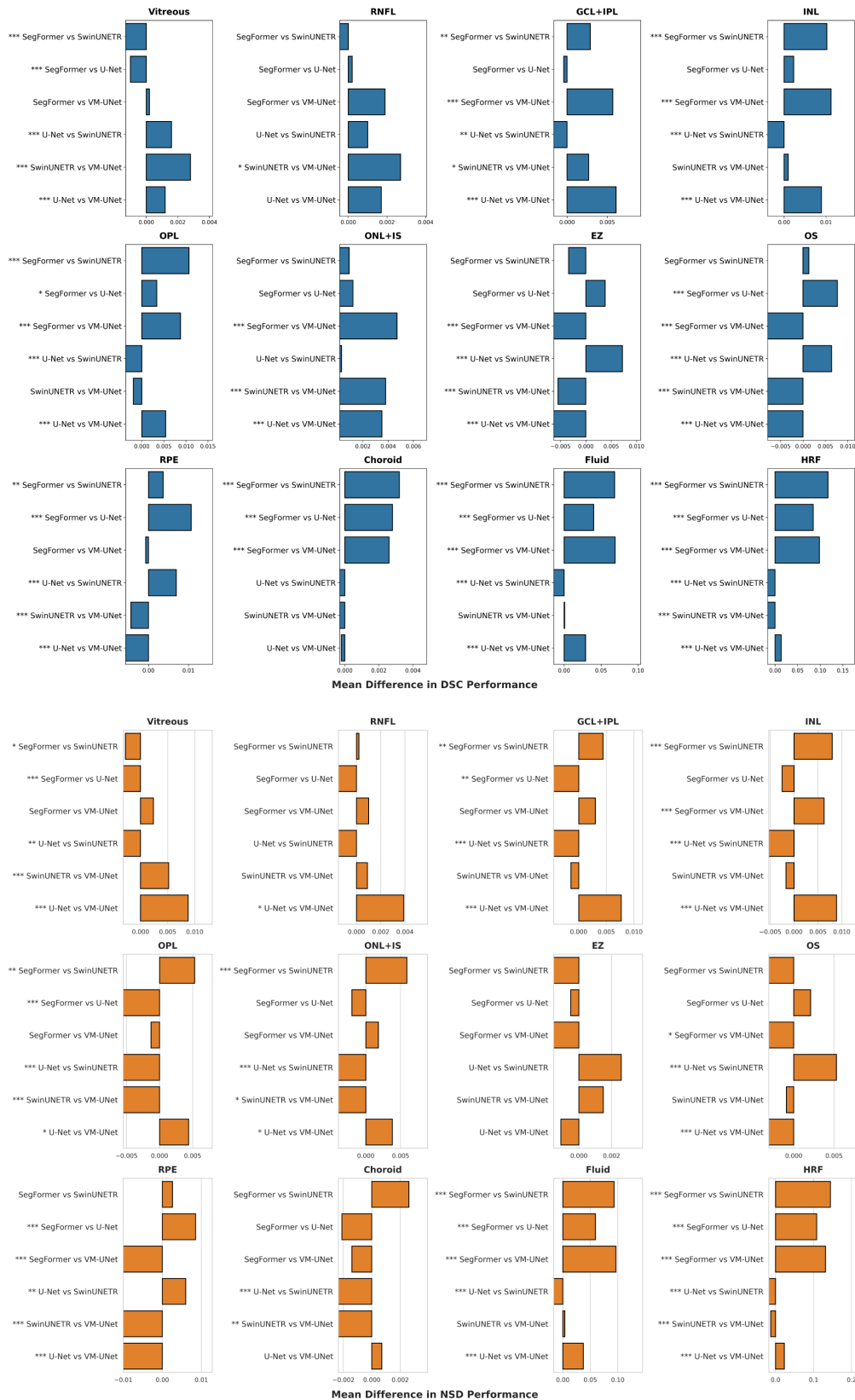
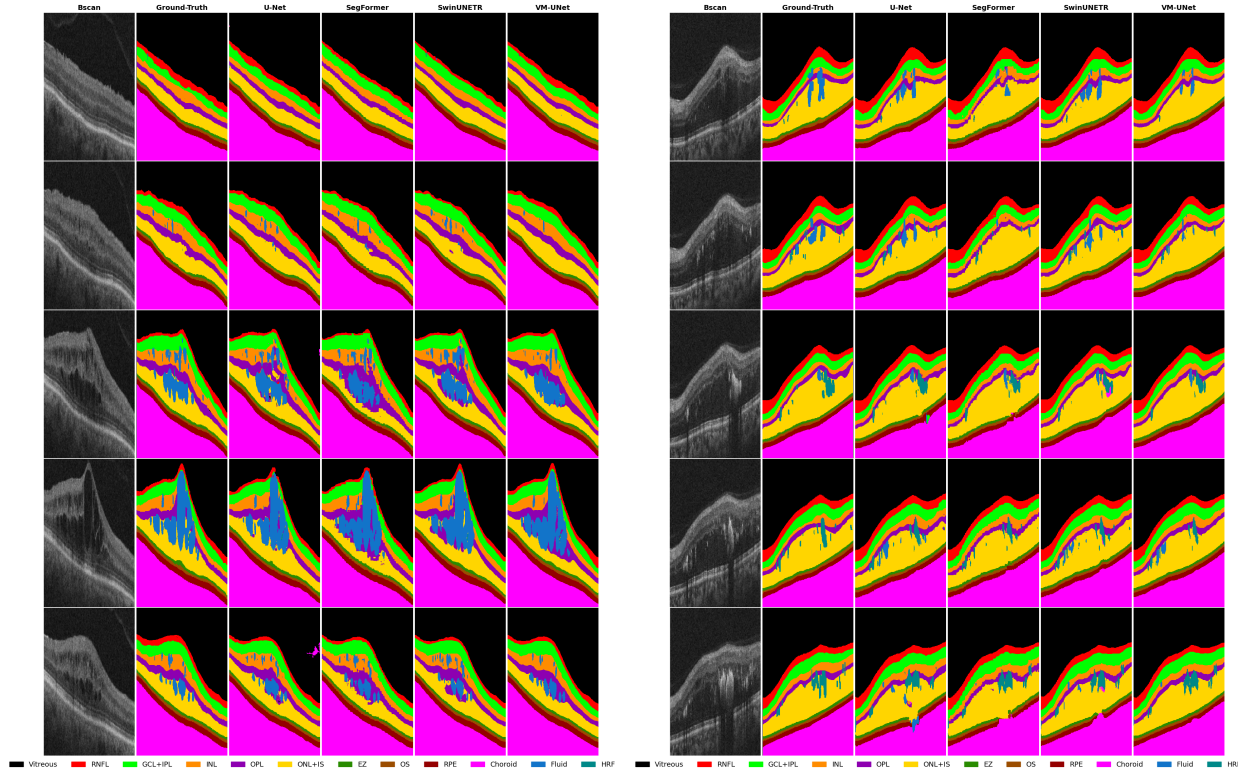
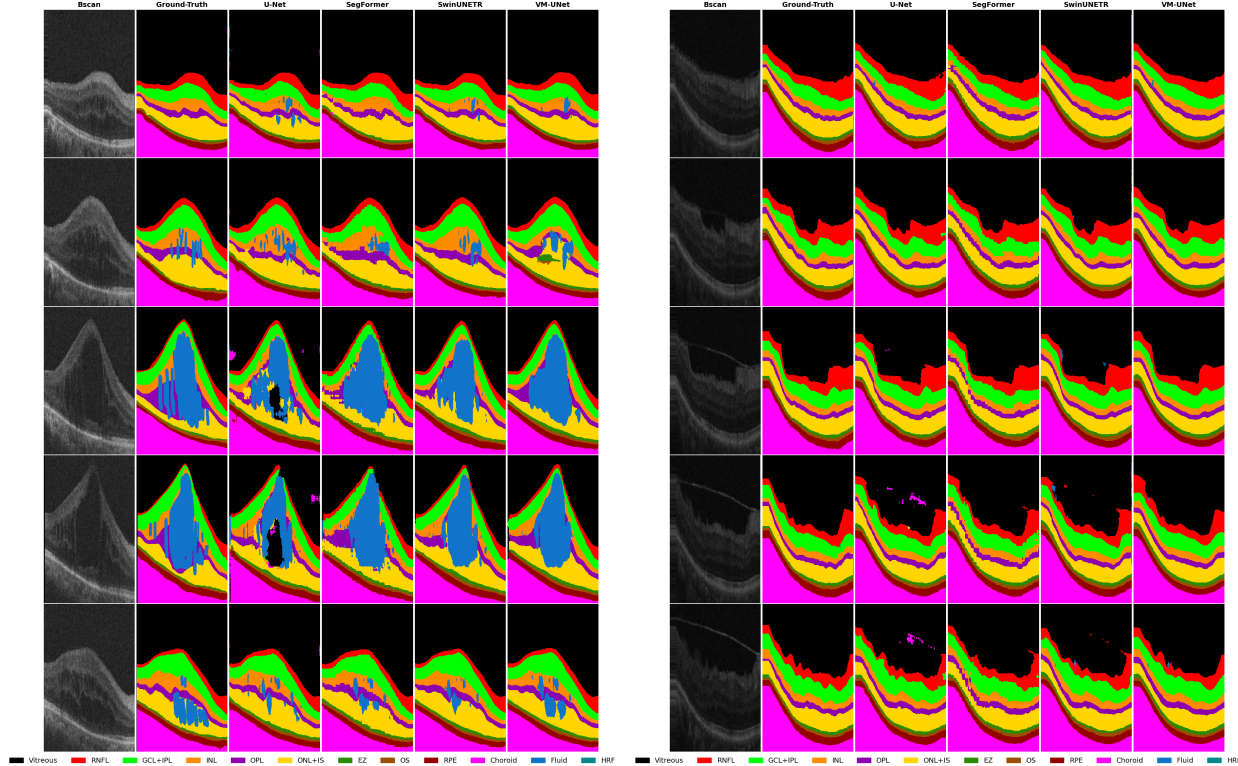


Fig. 4: Comparison of the mean difference of DSC and NSD scores between models for each retinal region. For each pair of models shown in the subplot, the mean difference is calculated by subtracting the mean of the first model from the second model. The marker before the name of each model pair indicates different significant levels(p-values) calculated by the Tukey HSD method. ***: $p < 0.001$, **: $p < 0.01$, *: $p < 0.05$, no marker: $p \geq 0.05$. Some barplots are invisible due to the limited precision of the mean difference.



(a) NPDR patient with severe fluid accumulation.

(b) NPDR patient with HRF and shading artifacts.



(c) PDR patient with severe fluid accumulation.

(d) PDR patient with partial retinal detachment.

Fig. 5: Comparison of OCT B-scan segmentation results across different retinal conditions. Each row represents a different B-scan, while columns correspond to different segmentation models and patient conditions.



Fig. 6: Comparison of USS(left) and OSS(right) for SwinUNETR and VM-UNet. Lower values indicate better segmentation performance.

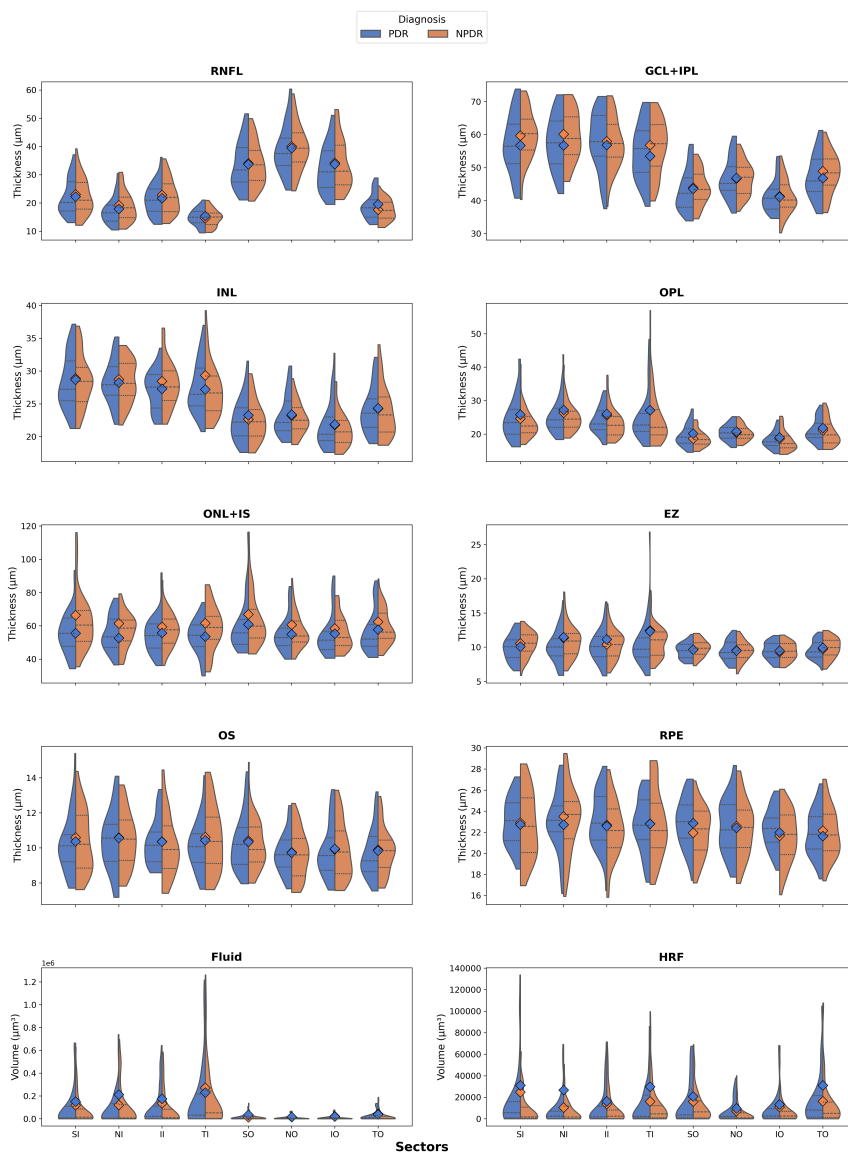
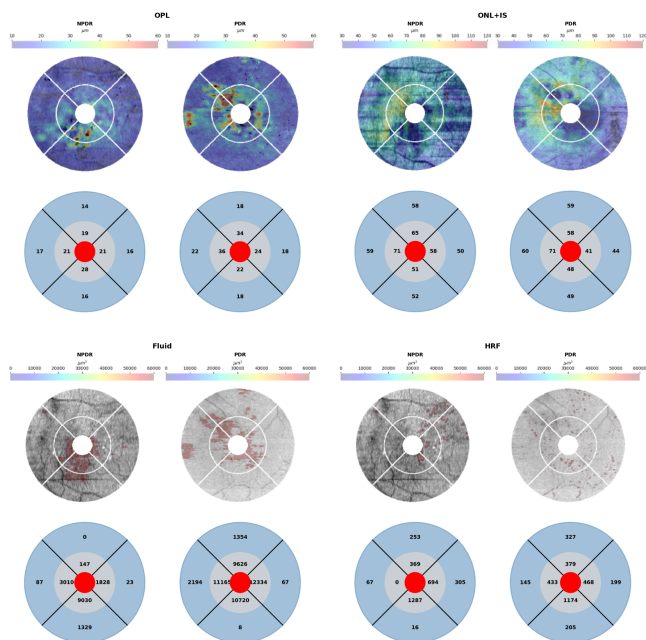
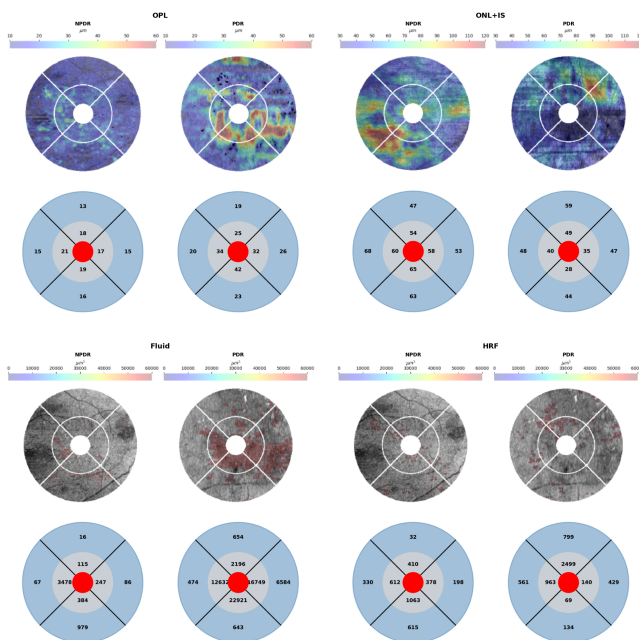


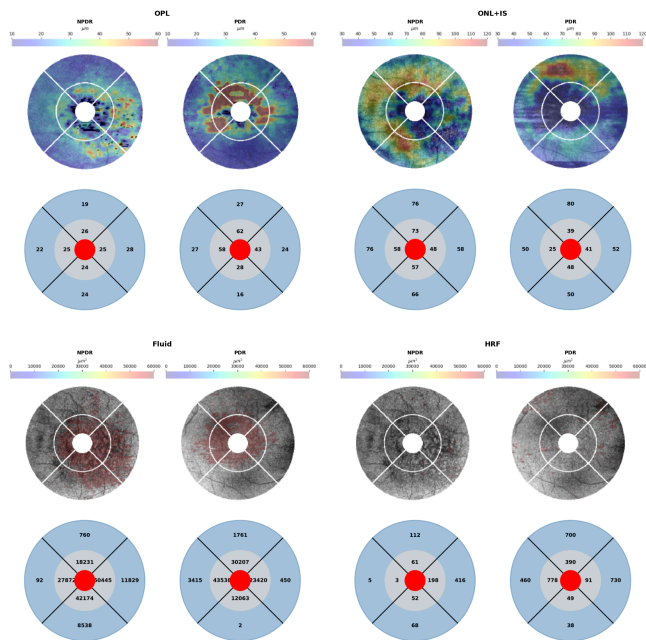
Fig. 7: The distribution of layer thickness and fluid volume measurements across different sectors for patients diagnosed with NPDR and PDR. The outliers are removed outside the 5th and 95th percentiles. The diamond markers represent the mean thickness for each group, calculated from the original data without outlier removal.



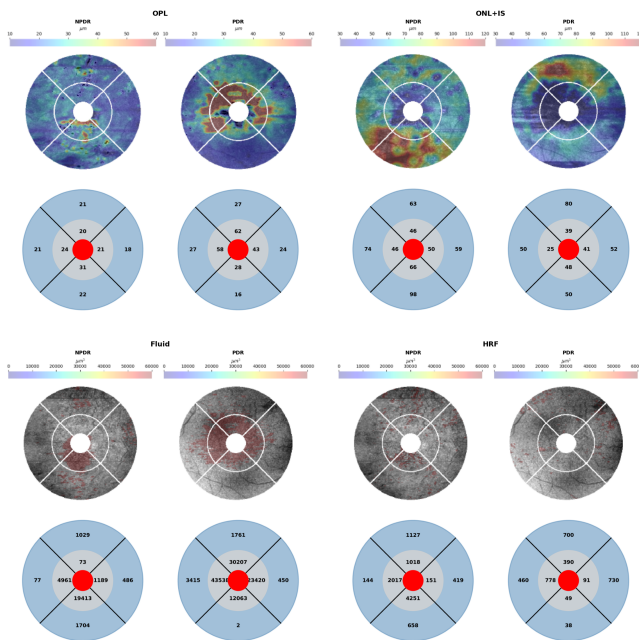
(a) Example of 57-year-old male patients with right eye image.



(b) Example of 54-year-old male patients with left eye image.



(c) Example of 59-year-old female patients with right eye image.



(d) Example of 59-year-old female patients with left eye image.

Fig. 8: Examples of ETDRS thickness map comparison between NPDR and PDR patient with matched age, gender and eyeside. For each region, the first row shows the thickness heatmap overlaid onto the layer En Face image. The second row shows the quantitative average thickness for each sector.